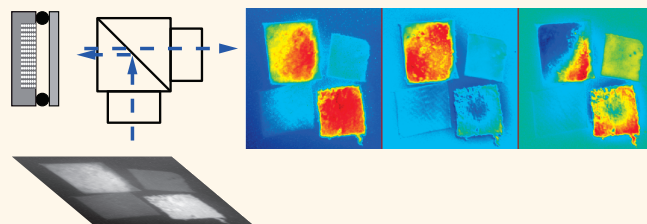


Thermally Modulated Porous Silica Multispectral Filters and Their Application in Remote Imaging

Adrian Garcia Sega,[†] Brian H. King,[†] Jessica Y. Lee,[†] Michael J. Sailor,[†] and Gordon M. Miskelly^{‡,*}

[†]Department of Chemistry and Biochemistry, University of California, San Diego, La Jolla, California 92093-0358, United States and [‡]School of Chemical Sciences, University of Auckland, Private Bag 92019, Auckland 1142, New Zealand

ABSTRACT We report a thermally tunable multispectral imaging filter based on reversible condensation of volatile organic fluids within a nanoporous one-dimensional photonic crystal. The photonic crystal (optical rugate filter) comprises oxidized porous silicon, prepared by electrochemical etch of silicon and subsequent air oxidation (porous silica rugate filter, pSiF). The reflectance spectrum of the pSiF is designed and constructed to match two of the red emission bands of the luminescent complex europium(III) tris-dipicolinate, $[\text{Eu}(\text{dpa})_3]^{3-}$, which has been used as an indicator for anthrax spores. When the pSiF is fitted with a thermoelectric Peltier cooler/heater and sealed in a container with 2-propanol vapor, microcapillary effects drive the temperature-dependent condensation/evaporation of 2-propanol into/out of the porous nanostructure. Thermal cycling experiments show that the wavelengths of the spectral bands of the pSiF are reversibly tuned by ± 35 nm for a temperature change of ± 40 °C. Difference images of a UV-illuminated scene containing the $[\text{Eu}(\text{dpa})_3]^{3-}$ target, obtained by reflection from pSiF that is continuously thermally cycled through the emission bands of the dye, show that the target can be discriminated from the background or from control targets with overlapping but dissimilar luminescence spectra.



KEYWORDS: porous silicon · free space imaging · anthrax · europium dipicolinate · luminescence · stand off detection · photonic crystal · microcapillary condensation

Multispectral and hyperspectral imaging systems that combine imaging and spectroscopy have applications in many fields including biomedicine,^{1,2} remote sensing,^{3,4} and land surveying.⁵ Hyperspectral imaging involves the generation of a spectrum for every pixel of the image, which can lead to extremely large data sets that can be cumbersome to analyze. For applications that do not require detailed spectral information, multispectral imaging can be utilized, where only key wavelengths are sampled for each pixel. For this imaging mode, the sampling of wavelengths is generally accomplished using fixed filters or a rapidly scanned optomechanical, acousto-optic, or electro-optic device.^{6–8} Selection of the appropriate wavelength filter involves trading issues such as cost, spectral resolution, wavelength range, spectral throughput, out of band rejection, susceptibility to mechanical failure, and speed. Recently, porous nanostructured photonic crystals have emerged as interesting candidates for tunable, high-resolution

spectral filters. Many tunable photonic systems can be found in biological systems, such as squid chromatophores and iridophores, which are tuned by the contraction of muscles,⁹ or the wings of certain butterfly species, which change color upon adsorption of water¹⁰ or organic molecules.¹¹ Porous silicon-based photonic crystals have been found to display a similar ability to change color, by adsorption of molecular species,¹² by mechanical deformation,¹³ or by thermal or electrical stimulation.^{14,15} Like many other inorganic photonic materials,^{16,17} these systems have an advantage over their biological counterparts in that they are readily manufactured into stable, durable, and reliable optical components suitable for multispectral imaging applications.

Current-modulated electrochemical etching of silicon has been used to prepare porous silicon rugate filters with narrow (fwhm ~ 10 nm) reflectance peaks.¹⁸ In addition, more complex electrochemical etching waveforms have been employed to generate

* Address correspondence to g.miskelly@auckland.ac.nz.

Received for review May 26, 2013 and accepted August 17, 2013.

Published online August 22, 2013
10.1021/nn402654z

© 2013 American Chemical Society

samples with multiple-peak reflectivity spectra.^{19–21} Previous work with porous silicon passband structures filled with liquid crystals demonstrated thermal and electrical tuning of the optical features, but wavelength changes were limited to <10 nm.^{15,22} Much larger changes in the position of the passband (>70 nm) have been achieved when the vapors of volatile liquids adsorb or condense within the porous silicon matrix,²³ and we reasoned that this reversible process could be used to prepare spectral filters tunable over a wide wavelength range. In this work, we show that thermal cycling of a porous silica rugate filter (pSiF) infiltrated with the volatile organic liquid 2-propanol can be used to reversibly shift the passband of the filter over a wavelength range in excess of 80 nm in the visible or near-infrared region of the spectrum. In addition, we show that the pSiF can be prepared with sufficient uniformity to allow multispectral imaging. We demonstrate a representative multispectral imaging application, involving identification of the distinctive luminescence signature of the chemical species dipicolinate (dpa) complexed to europium ($[\text{Eu}(\text{dpa})_3]^{3-}$). The species dpa is associated with anthrax spores, and lanthanide complexes of dpa have been used as an indicator for anthrax spores.²⁴ The sensitivity of this approach arises from the fact that most Eu(III) salts display very weak luminescence, but dpa acts as a sensitizer for luminescence from the f-orbital levels in the lanthanide, increasing the luminescence intensity by a factor of more than 10^3 .²⁵

RESULTS AND DISCUSSION

Construction of Thermally Tunable Optical Filters. The porous silica rugate filter was prepared using the electrochemical etching method typically employed to prepare porous Si rugate filters,²⁶ with care taken to provide an optically uniform response over the central region of 12.5 mm diameter. The method involves etching a silicon

wafer with a sinusoidal electrochemical current waveform. The period of the sinusoid determines the spectral wavelength of the passband, and a composite electrochemical current waveform consisting of two (or more) superimposed sinusoids will generate a rugate filter with two (or more) passbands. Because of the differing widths of the Eu emission bands, the shorter wavelength peak was constructed using two sinusoids with similar periods in the composite waveform. This generated a relatively broad, single passband. A third sinusoid with a significantly different period was also included in the composite waveform to generate the second passband. Scanning electron microscope (SEM) images of the porous silicon surface and cross section (Supporting Information) confirmed the porous morphology.

The porous silicon was then thermally oxidized to porous silica to provide improved environmental stability. Our previous studies on condensation of volatile liquids into porous silica suggested that 2-propanol would be suitable for this imaging filter application.²⁷ Absorption of 2-propanol vapor into the porous matrix is quite reversible, although the time response of the desorption process at room temperature is slow, and a flow-based dosing system was thought to be too cumbersome and slow to be practical for a spectral imaging system. Instead, we added a fixed amount of 2-propanol to the pSiF sample chamber and controlled the extent of adsorption and capillary condensation by controlling the temperature of the porous silica, Figure 1. A Peltier device fixed to the backside of the wafer containing the pSiF provided both active heating and cooling. This approach allows the optical apparatus to be sealed and compact. Experimentally, we found that the passband wavelength drifted slightly during the first three temperature cycles, but subsequent cycles yielded stable and consistent values for the passband wavelengths over the complete thermal cycle. The imaging results

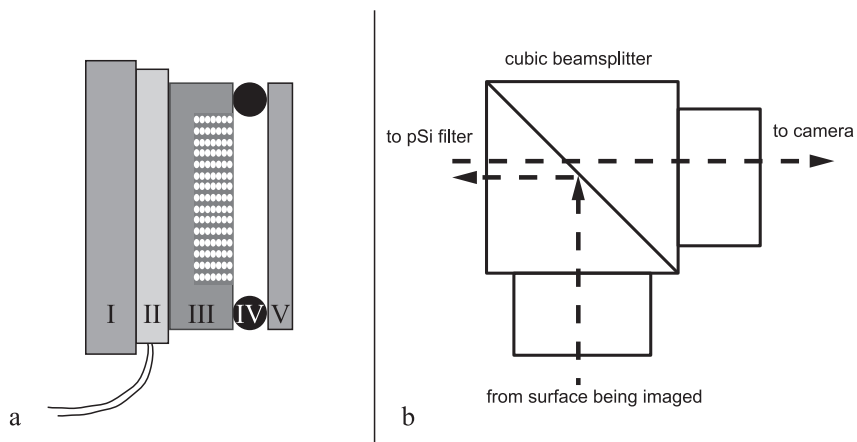


Figure 1. (a) Schematic of porous silica filter cell and sample chamber. (I) Copper heat sink, (II) Peltier device, (III) porous silica filter on silicon wafer substrate, (IV) seal for the sample chamber, (V) glass cover-slide. The entire filter cell has no moving parts. (b) Schematic of optical setup used for imaging. Lenses were placed between the beamsplitter and the camera and between the surface being imaged and the beamsplitter to adjust for field of view and working distance.

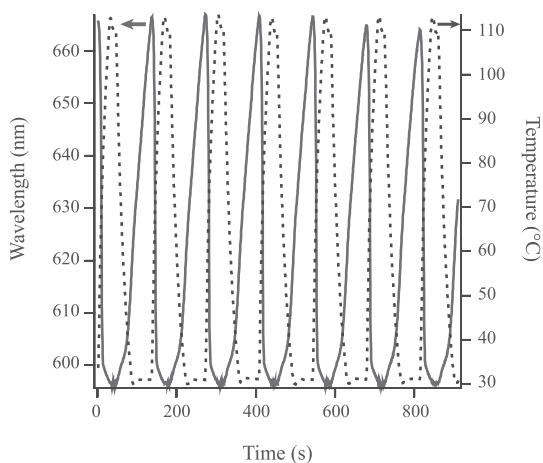


Figure 2. Graph showing the wavelength of the main reflectance maximum of the porous silica rugate filter (pSiF, solid curve) and the corresponding temperature of the pSiF sample (dashed curve) as a function of time. The pSiF was sealed in the presence of 95 parts per thousand of 2-propanol, and it was heated and cooled through seven cycles.

presented in this paper are from the fourth and subsequent cycles.

Thermal Behavior of Tunable Porous Silica Optical Filter. The optical response of the filter as a function of temperature was initially characterized using a spectrophotometer with a reflectance probe. When the sample cell contained 95 parts per thousand of 2-propanol, a shift of ~ 70 nm in the position of the rugate band maximum was measured upon continuous cycling of the temperature between *ca.* 30 and 110 °C (Figure 2). Relative to the high-temperature phase of the cycle, the low-temperature phase corresponds to a condition in which a greater fraction of the 2-propanol in the cell was condensed into the porous silica, which caused the observed red shift in the wavelength of the passband maximum. A plot of this wavelength as a function of time shows the same periodicity as the temperature *versus* time plot, but with a significant time lag and alteration in shape, Figure 2.

The observed responses are attributed to temporal differences between heat transfer and mass transfer processes to and within the porous nanostructure. Heat transfer is rapid in porous Si systems due to their good thermal conductivity^{28,29} (although this will be reduced upon partial reduction to silica), whereas the mass transport of 2-propanol into and out of the nanoporous matrix is slower. A plot of the wavelength of the passband maximum as a function of temperature (Figure 3) shows that during the heating phase of the cycle most 2-propanol is lost once the temperature of the pSiF exceeds 60 °C, while on cooling, significant readsorption occurs only below 40 °C, with most capillary condensation occurring once the pSiF has reached its lowest temperature. It should be noted that the Peltier heater/cooler causes a slight overshoot at each end of the temperature range, but this is

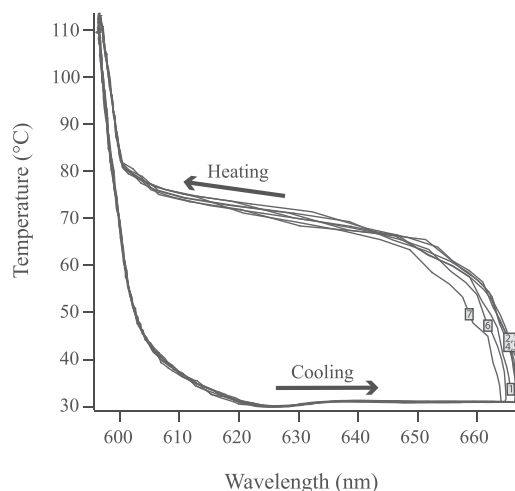


Figure 3. Plot of temperature *vs* the wavelength of the main reflectance maximum of the pSiF over seven heating and cooling cycles, showing the hysteresis of the reflectance response. Numbers refer to consecutive cycles.

reproducible and does not affect the response of the pSiF in the wavelength range of interest.

Imaging with a Thermally Tunable Silica Optical Filter: Exploratory Data Analysis. Next, the pSiF was evaluated as a multispectral tunable imaging filter. The pSiF was placed in the optical path of the imaging system as depicted in Figure 1. The optics were focused on a set of glass fiber pad targets infused with either the analyte or various controls: the analyte, luminescent $[\text{Eu}(\text{dpa})_3]^{3-}$; a control that contained $\text{Eu}(\text{NO}_3)_3$ with no added ligands; a luminescent interferent, the dye $[\text{Ru}(\text{DMB})_3]^{2+}$, which has an intense but broad luminescence; and a blank control that consisted of a clean glass fiber pad as shown in Figure 4. The images show slight brightness variations due to illuminant non-uniformity and vignetting from the imaging components, but these were sufficiently minor that they were not corrected prior to image analysis. The luminescence spectra of $[\text{Eu}(\text{dpa})_3]^{3-}$ and $[\text{Ru}(\text{DMB})_3]^{2+}$ are shown in Figure 4d, together with reflectance spectra of the pSiF at three different points during a thermal cycle.

The experimental runs were designed so that the analysis started with rapid heating of the pSiF to the maximum temperature, followed by slow cooling, with images being acquired throughout the heating and cooling phases. Each image was processed with 3×3 spatial averaging to reduce the effect of non-uniformity in pixel response. The design of the pSiF imager meant that we could not obtain an unfiltered image of the targets under identical conditions, and so instead an image of the mean luminescence over a whole thermal cycle was calculated, Figure 5a, to represent what would be observed with no filter. The $[\text{Ru}(\text{DMB})_3]^{2+}$ target in this image is slightly brighter than the $[\text{Eu}(\text{dpa})_3]^{3-}$ partly because the former complex is luminescent over a greater portion of the thermal cycle (wavelength range scanned). An image

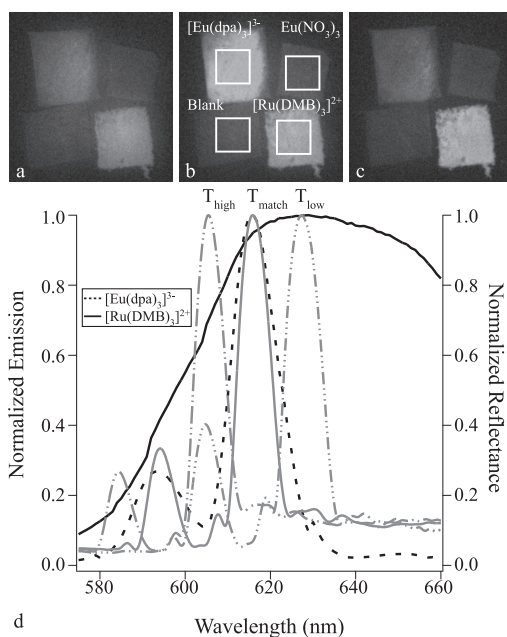


Figure 4. Images and emission spectra of glass fiber filter targets acquired during continuous thermal cycling of the porous silica rugate filter (pSiF). The four targets in the images are (clockwise from top left) glass fiber filters containing $[\text{Eu}(\text{dpa})_3]^{3-}$, the nonchelated $\text{Eu}(\text{NO}_3)_3$, the luminescent complex $[\text{Ru}(\text{DMB})_3]^{2+}$, and a blank control. The white squares shown in image panel b are 86×86 pixel ROIs used in quantification of the target responses (*vide infra*). (a) Image obtained with the pSiF tuned to the blue of the emission maximum of $[\text{Eu}(\text{dpa})_3]^{3-}$ (Image_{T_{high}}). (b) Image obtained with the pSiF tuned to match the emission of $[\text{Eu}(\text{dpa})_3]^{3-}$ (Image_{T_{match}}). (c) Image obtained with the pSiF tuned to the red of the emission maximum of $[\text{Eu}(\text{dpa})_3]^{3-}$ (Image_{T_{low}}). (d) Plot showing the luminescence spectra of the two complexes $[\text{Eu}(\text{dpa})_3]^{3-}$ and $[\text{Ru}(\text{DMB})_3]^{2+}$ and the reflectance spectra of the pSiF obtained at three temperatures: T_{high} , higher temperature (ca. 80 °C) corresponding to image a; T_{match} , temperature corresponding to the best match of the pSiF reflectance with the main emission band of $[\text{Eu}(\text{dpa})_3]^{3-}$ (ca. 60 °C, image b); T_{low} , lower temperature (ca. 40 °C) corresponding to image c. The reflectance and luminescence spectra were collected in a 90° backscatter configuration using an Ocean Optics USB4000 CCD spectrophotometer.

taken when the pSiF optical filter reflectivity maximum matches the emission maximum of $[\text{Eu}(\text{dpa})_3]^{3-}$ (Image_{T_{match}}, Figure 5b) shows a slightly greater luminescence for $[\text{Eu}(\text{dpa})_3]^{3-}$ than for $[\text{Ru}(\text{DMB})_3]^{2+}$. This result indicates that using a narrow-band filter with a bandpass overlapping the 615 nm maximum for $[\text{Eu}(\text{dpa})_3]^{3-}$ does provide increased selectivity, but it also shows that attempts at detection of $[\text{Eu}(\text{dpa})_3]^{3-}$ with a single filter can result in interferences from other luminescent materials.

Figure 6 shows a plot of the integrated intensity from an 86×86 pixel region in the center of the $[\text{Eu}(\text{dpa})_3]^{3-}$ target as a function of time, through five continuous heat/cool cycles of the pSiF. The shape of the integrated intensity–time trace is different compared to the spectrophotometric measurement of the wavelength of the maximum of the main pSiF reflectance band in Figure 2 because the increase in luminescence intensity

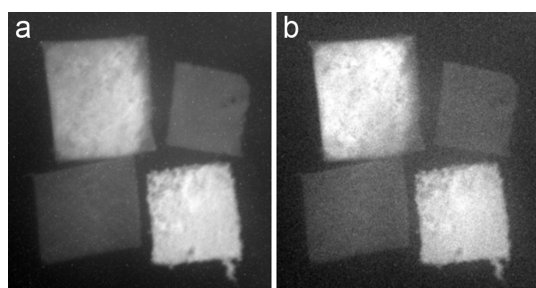


Figure 5. (a) Average of images acquired over one complete heating and cooling cycle of the pSiF. (b) Image obtained when the pSiF reflectance wavelength matches the peak emission wavelength of $[\text{Eu}(\text{dpa})_3]^{3-}$ (Image_{T_{match}}).

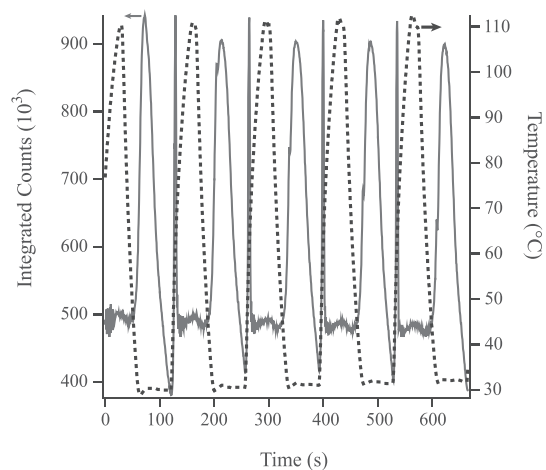


Figure 6. Plot showing the integrated pixel intensities calculated from the ROI of the luminescent $[\text{Eu}(\text{dpa})_3]^{3-}$ target (see Figure 4b for location) as a function of time during five heat/cool cycles (solid curve). The temperature of the pSiF as measured with a thermocouple contact probe is shown as the dashed curve. The selected images shown in Figures 4a–c and discussed in the difference imaging section were acquired during the heating phase, which appears as the sharp spike in each cycle of the luminescence response on this time scale.

in Figure 6 occurs when the main reflectivity maximum of the pSiF overlaps with the 615 nm emission band of the $[\text{Eu}(\text{dpa})_3]^{3-}$ target. The sharp spike in the observed intensity during the heating phases in Figure 6 is due to the fast desorption of 2-propanol upon heating of the pSiF, which in turn leads to a rapid blue shift in the wavelength of the reflectance maximum of the pSiF past the 615 nm emission band of $[\text{Eu}(\text{dpa})_3]^{3-}$.

Principal component analysis (PCA) of the images obtained during a complete single thermal cycle was performed to characterize the ability of the pSiF to discriminate between the targets. The PCA treated each pixel as an individual sample, with the intensity at each time point (image) in the thermal cycle being the dependent variables (images were collected at 2 Hz during the cycle). Three principal components were retained as explaining most of the variability in the images, with PC1, PC2, and PC3 explaining 99.37%, 0.37%, and 0.12% of the total variability in the images,

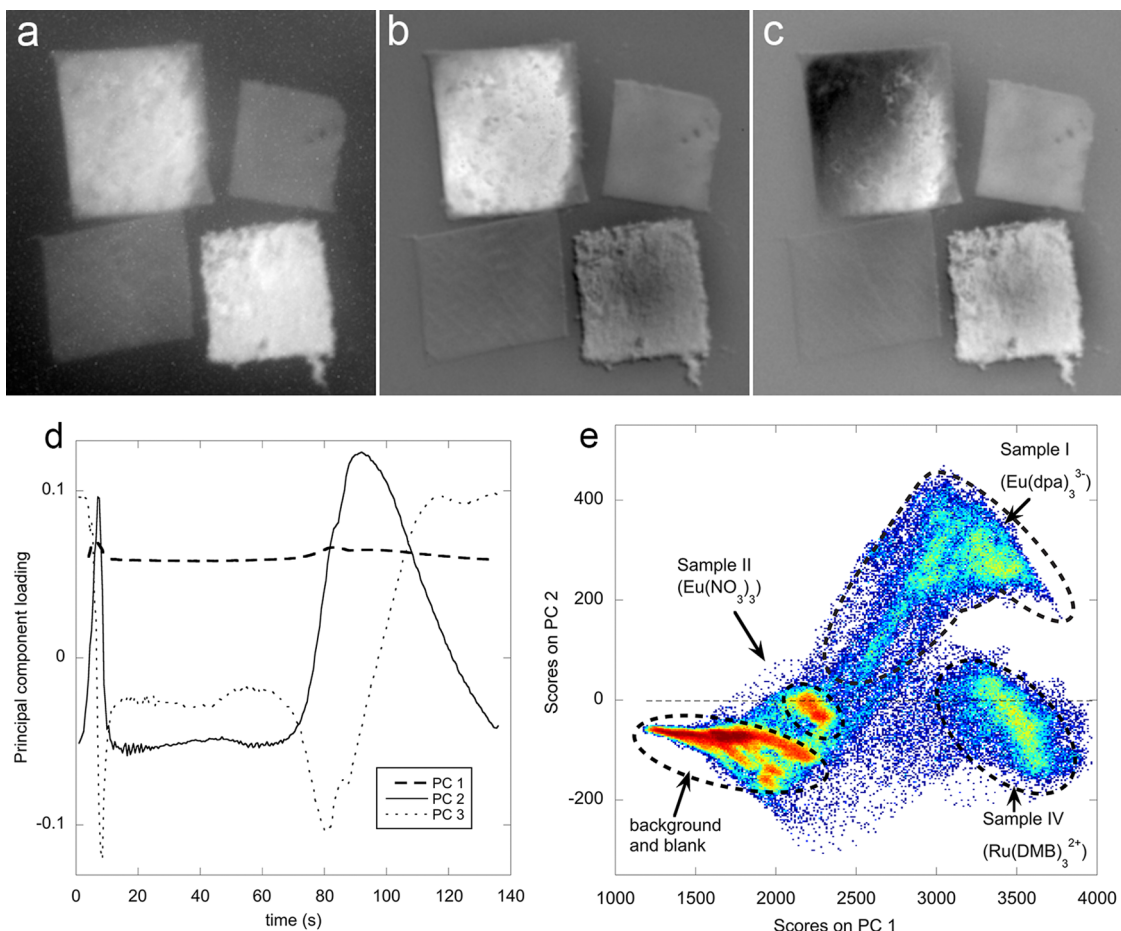


Figure 7. Results from principal component analysis of the images collected during one heat/cool cycle of the pSiF. (a–c) Images in which the brightness at each pixel indicates the scores corresponding to principal components 1 through 3, respectively. (d) Loadings of each principal component as a function of the time during a heat/cool cycle. (e) Scatter plot showing the scores on the first and second principal components of all the pixels in the imaged area. The color coding in (e) is according to the density of pixels at a given location on the graph (red is highest density).

respectively. The PCA was performed without any pre-processing of the images other than the 3×3 spatial averaging because this led to the second principal component aligning with the direction of greatest difference between the $[\text{Eu(dpa)}_3]^{3-}$ target and the remainder of the scene, Figure 7. The first principal component correlated closely with the average luminescence intensity throughout the whole thermal/spectral tuning cycle, and the $[\text{Ru(DMB)}_3]^{2+}$ complex gave a slightly stronger response than did the $[\text{Eu(dpa)}_3]^{3-}$ in an image of the scores of this principal component, Figure 7a. As expected, this image has a similar visual appearance to the average image shown in Figure 5a. The $[\text{Eu(dpa)}_3]^{3-}$ target was bright in the image corresponding to the scores of the second principal component, Figure 7b, with the nonchelated $\text{Eu}(\text{NO}_3)_3$ also showing a small positive response. The loadings of the images on the second principal component (Figure 7d) show that it has positive contributions from images around 8 s and 70–120 s after a heat/cool cycle is initiated and negative contributions elsewhere. These regions of positive contribution correspond with the

maxima observed in Figure 5 and with the pSiF reflectance band matching the peak emission wavelength for $[\text{Eu(dpa)}_3]^{3-}$ (ca. 615 nm) in Figure 4. Interestingly, the principal component analysis showed that the $[\text{Eu(dpa)}_3]^{3-}$ target did not have a completely spatially uniform luminescent response during the thermal cycling, with the image of the scores for principal component 3 showing a gradation out from the center of the image, Figure 7c. In agreement with this observation, the dominant features in the loadings plot of principal component 3 show a differential relationship compared to the loadings of principal component 2. This effect is probably due to a very slight shift in peak wavelength of the rugate reflectance band across the pSiF.

A scatter plot showing the scores of all the pixels from the imaged area on principal components 1 and 2, Figure 7e, shows clear discrimination of the pixels corresponding to the glass fiber filters coated with $[\text{Eu(dpa)}_3]^{3-}$, $\text{Eu}(\text{NO}_3)_3$, and $[\text{Ru(DMB)}_3]^{2+}$ from the background and the blank filter. This plot shows that, as stated earlier, the use of noncentered image data results in principal component 2 lying along the

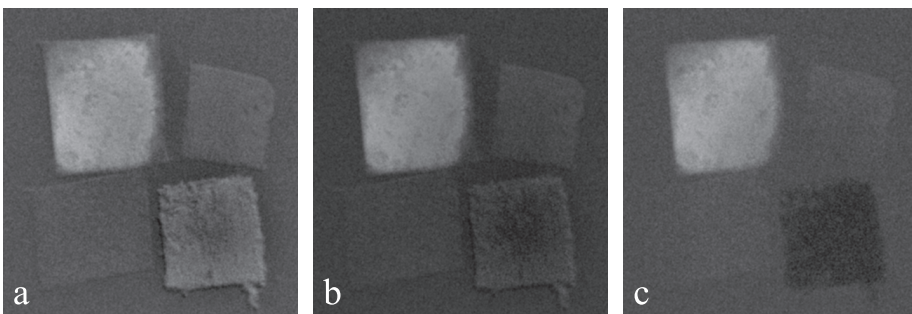


Figure 8. Calculated images resulting from the three difference imaging procedures: (a) $\text{Image}_{T_{\text{match}}} - \text{Image}_{T_{\text{high}}}$; (b) $\text{Image}_{T_{\text{match}}} - 0.5 \times (\text{Image}_{T_{\text{high}}} + \text{Image}_{T_{\text{low}}})$; (c) $\text{Image}_{T_{\text{match}}} - \text{Image}_{T_{\text{low}}}$.

direction that best discriminates the pixels corresponding to the $[\text{Eu}(\text{dpa})_3]^{3-}$ target from the pixels corresponding to all other parts of the image. The outlying data points for each region in Figure 7e correspond to pixels around the edges of each glass fiber target.

Imaging with a Thermally Tunable Silica Optical Filter: Difference Imaging. The intensity changes for the $[\text{Eu}(\text{dpa})_3]^{3-}$ target during continuous thermal cycling shown in Figure 6 and the loadings plot for the second principal component (Figure 7d) suggest that the $[\text{Eu}(\text{dpa})_3]^{3-}$ target can be enhanced relative to the remainder of the scene by taking information from as few as two or three images taken when the pSiF reflectance maximum coincides with $\text{Image}_{T_{\text{match}}}$ and is near but not overlapping with the $[\text{Eu}(\text{dpa})_3]^{3-}$ emission ($\text{Image}_{T_{\text{high}}}$ and $\text{Image}_{T_{\text{low}}}$). This background correction approach using differences of images has been described previously in a forensic context.³⁰ Thus, the three images of the target set shown in Figure 4 were used for further processing. Images a, b, and c in Figure 4 were obtained during the heating part of a thermal cycle when the temperature of the pSiF was approximately 80, 60, and 40 °C and are termed $\text{Image}_{T_{\text{high}}}$, $\text{Image}_{T_{\text{match}}}$, and $\text{Image}_{T_{\text{low}}}$ respectively, in the following discussion. An image ($\text{Image}_{T_{\text{match}}}$) taken with the pSiF bandpass centered at the 615 nm peak emission wavelength for $[\text{Eu}(\text{dpa})_3]^{3-}$ shows luminescence from this Eu complex and from $[\text{Ru}(\text{DMB})_3]^{2+}$, with very little emission from the background or uncomplexed Eu. An image ($\text{Image}_{T_{\text{low}}}$) taken with the pSiF bandpass positioned at longer wavelengths than the $[\text{Eu}(\text{dpa})_3]^{3-}$ emission maximum shows little emission from $[\text{Eu}(\text{dpa})_3]^{3-}$, but it has significant luminescence from $[\text{Ru}(\text{DMB})_3]^{2+}$, while an image ($\text{Image}_{T_{\text{high}}}$) with the pSiF bandpass positioned at a slightly shorter wavelength than the $[\text{Eu}(\text{dpa})_3]^{3-}$ emission maximum showed little luminescence from any target in the image. Three difference image procedures using these three images were examined. In the most effective procedure, a corrected image was calculated by subtracting the average of the images taken at the two bracketing wavelengths ($\text{Image}_{T_{\text{high}}}$ and $\text{Image}_{T_{\text{low}}}$) from the image taken at a temperature where the pSiF main reflectance band was centered on the same wavelength as the emission of $[\text{Eu}(\text{dpa})_3]^{3-}$

($\text{Image}_{T_{\text{match}}}$), Figure 8b. This image calculation corresponds to eq 1 in the Experimental Section and enhances narrow luminescence bands within the defined spectral region compared to broad features. The $[\text{Eu}(\text{dpa})_3]^{3-}$ target is greatly enhanced relative to the remainder of this difference image, so that good selectivity is achieved.

Selective enhancement of the $[\text{Eu}(\text{dpa})_3]^{3-}$ relative to the $[\text{Ru}(\text{DMB})_3]^{2+}$ could also be achieved by subtracting only the longer wavelength image ($\text{Image}_{T_{\text{low}}}$) from that centered at the $[\text{Eu}(\text{dpa})_3]^{3-}$ emission ($\text{Image}_{T_{\text{match}}}$), Figure 8c (eq 2). Indeed, since the $[\text{Ru}(\text{DMB})_3]^{2+}$ has increased emission at the longer wavelength, it appears darker than the background in this image. Both the $[\text{Eu}(\text{dpa})_3]^{3-}$ and $[\text{Ru}(\text{DMB})_3]^{2+}$ are visible in the difference image calculated by subtracting only the shorter wavelength image ($\text{Image}_{T_{\text{high}}}$) from the image taken centered on the emission of the $[\text{Eu}(\text{dpa})_3]^{3-}$ ($\text{Image}_{T_{\text{match}}}$), Figure 8a. Since interfering luminescences could have emission spectra with maxima at any position relative to the emission maximum of the analyte, this last result indicates that the subtraction of a single image taken at a nearby wavelength to correct for the effects of interfering luminescence on the emission from the target analyte can lead to false positive results. However, the difference image calculated by subtraction of the average of two bracketing bandpass images (Figure 8b) is more robust toward such errors.

In order to quantify the effects of the above background correction procedures, a region of interest (ROI) of area 86×86 pixels was located on each target as shown in Figure 4, and the intensity values for each pixel in the ROI of the difference images in Figure 8 were integrated, Table 1. The integrated intensities in each ROI are given together with standard deviations determined from separate measurements from five sequential heat/cool cycles. The selectivity ratios in Table 1 are the ratios between the mean value for the intensity of the $[\text{Eu}(\text{dpa})_3]^{3-}$ target and the mean intensity values for the other targets. The selectivity ratios of the $[\text{Eu}(\text{dpa})_3]^{3-}$ target to the blank and to the $[\text{Ru}(\text{DMB})_3]^{2+}$ target are greater than 3 when the difference image calculated by subtracting the average

TABLE 1. Integrated Pixel Intensity (divided by 10^3) of a 86×86 Pixel Square of Each Sample Swatch ($[\text{Eu}(\text{dpa})_3]^{3-}$, blank, $\text{Eu}(\text{NO}_3)_3$, $[\text{Ru}(\text{DMB})_3]^{2+}$, see Figure 4) from Images That Have Been Corrected Using the Three-Image and Two-Image Differencing Procedures^a

	$[\text{Eu}(\text{dpa})_3]^{3-}$	blank	$\text{Eu}(\text{NO}_3)_3$	$[\text{Ru}(\text{DMB})_3]^{2+}$
$\text{Image}_{T_{\text{match}}} - 0.5 \times (\text{Image}_{T_{\text{high}}} + \text{Image}_{T_{\text{low}}})$	842 ± 14	263 ± 13	321 ± 47	213 ± 26
$\text{Image}_{T_{\text{match}}} - \text{Image}_{T_{\text{high}}}$	990 ± 27	434 ± 20	525 ± 42	518 ± 32
$\text{Image}_{T_{\text{match}}} - \text{Image}_{T_{\text{low}}}$	968 ± 30	366 ± 29	391 ± 38	181 ± 11
		SR	2.65	2.48
				5.35

^a Standard deviations are derived from calculating the integrated pixel intensities separately for images corresponding to five consecutive heat/cool cycles. The selectivity ratio (SR) is the ratio of the response for $[\text{Eu}(\text{dpa})_3]^{3-}$ to that for each of the other targets.

of $\text{Image}_{T_{\text{high}}}$ and $\text{Image}_{T_{\text{low}}}$ is used, while the nonsensitized europium has a selectivity ratio slightly less than 3. The selectivity ratio values for the blank and $\text{Eu}(\text{NO}_3)_3$ ROIs that are calculated for the other two correction methods are slightly smaller, indicating less discrimination between the desired analyte and these other targets. Although the selectivity ratio for $[\text{Ru}(\text{DMB})_3]^{2+}$ was increased in one of the single difference images ($\text{Image}_{T_{\text{match}}} - \text{Image}_{T_{\text{low}}}$), the decreased selectivity ratio for the other single difference image ($\text{Image}_{T_{\text{match}}} - \text{Image}_{T_{\text{high}}}$) indicates that difference imaging using only a single image taken at a nearby wavelength for the correction is only useful if information about the relative wavelengths of the emission maxima of the analyte and luminescent interferences being imaged is known beforehand. In contrast the three-image difference method (eq 1) requires only knowledge of the wavelength of the analyte emission maximum and the fact that the analyte emission is narrow compared to the emission spectra of the interferences.

An alternative representation of the ability of the pSiF and data analysis to selectively identify the $[\text{Eu}(\text{dpa})_3]^{3-}$ target is using ROC curves, showing the fraction of target pixels correctly identified (true positives) *versus* the fraction of nontarget pixels identified as target pixels (false positives). The ROC curves were calculated by selecting all the pixels corresponding to the glass fiber filter with $[\text{Eu}(\text{dpa})_3]^{3-}$ as the target and all other pixels as being nontarget. As shown in Figure 9, the three-wavelength correction and the scores plot for principal component 2 using this definition of the target had $p(\text{true positive}) = 0.93$ and 0.88, respectively, when $p(\text{false positive}) = 0.01$. Thus, the three-wavelength correction (based on only three images) outperforms the principal component 2 scores images (based on 271 images over a complete heat/cool cycle). Since the glass fiber sample did not have a uniform distribution of $[\text{Eu}(\text{dpa})_3]^{3-}$ across the whole surface, we also plotted the ROC curve when only the ROI for the $[\text{Eu}(\text{dpa})_3]^{3-}$ target (top left

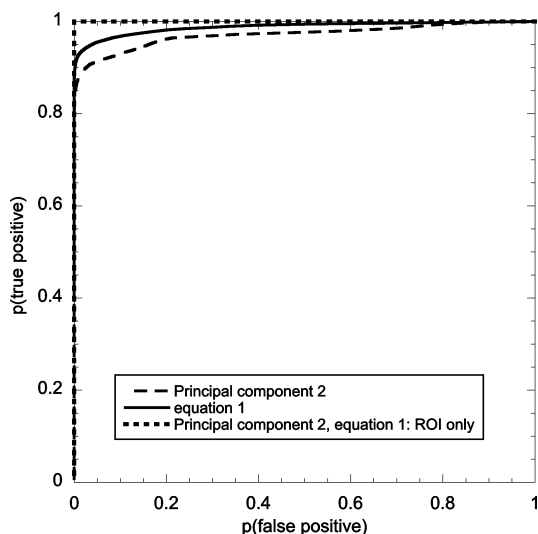


Figure 9. ROC curves for detection of $[\text{Eu}(\text{dpa})_3]^{3-}$ based on either the scores image for principal component 2 from the PCA or the difference image calculated according to eq 1. When the target region was specified as the region of interest (ROI) within the $[\text{Eu}(\text{dpa})_3]^{3-}$ sample (see Figure 4b) and the nontarget region was specified as all pixels outside the glass fiber coated with $[\text{Eu}(\text{dpa})_3]^{3-}$, then classification was almost perfect for both principal component 2 and the difference image, with their ROC curves overlapping. The other two ROC curves are based on the target region being the whole glass fiber sample coated with $[\text{Eu}(\text{dpa})_3]^{3-}$.

rectangle in Figure 4b) was used to evaluate the true positives and pixels corresponding to the whole scene except for the $[\text{Eu}(\text{dpa})_3]^{3-}$ glass fiber sample were used to evaluate the false positives. In this case the ROC curve showed 100% correct identification with no false positives (Figure 9).

Comparison with Other Multispectral Filter Systems. In general, imaging systems with fixed filters have the advantage of narrow passbands and high throughput, but are limited in the number of bands they can sample. Thin film multispectral fixed filters can be readily fabricated by depositing repeating layers of varying refractive indices; however, adding multiple transmission bands or varying the percent transmission of each individual passband can reduce the overall transmittance of the filter.³¹ An alternative method to sample multiple wavelengths is to use a scanning filter such as a Fabry–Perot etalon. In theory, etalons have a wide spectral range, but are practically limited by the stepping size of their motors.³² Because both filter wheels and scanned filters contain moving parts, they can be susceptible to physical damage. When rapid and reproducible wavelength selection over large wavelength ranges is required, liquid crystal tunable filters (LCTF) or acousto-optic tunable filters (AOTF) can be used. While based on differing principles, they both can scan a single passband with a moderate imaging aperture.⁸ The major drawbacks of these filter types are their cost and that LCTF devices cannot sample multiple wavelengths simultaneously. The pSiF structure investigated

in this work contains some of the advantages of both tunable and fixed filter systems. Like a fixed filter, the device can be manufactured to match a simple or complex spectral pattern, while like a LCTF or AOTF these spectral features can be tuned over a wide range. A drawback of the present system is that the spectral features of the device are tuned by thermal stimulation, necessitating good temperature control to allow reproducible performance.

CONCLUSIONS

In this work we demonstrate that a porous silica rugate filter, infused with 2-propanol vapors, can act as a thermally tunable optical filter with a temperature response of $\sim 1 \text{ nm}/^\circ\text{C}$ in the temperature range $30\text{--}115 \text{ }^\circ\text{C}$. We show that this system can identify a specific spectral target, a luminescent lanthanide complex. The sharp spectral features of the porous Si rugate filter allow excellent identification of the distinctive spectrum of the lanthanide complex $[\text{Eu}(\text{dpa})_3]^{3-}$. The more distinct the spectral features of the target are from those of either background or interferences are, the easier it will be to distinguish the target using the procedures described in this paper. A difference image obtained by subtracting an image taken when the pSiF reflectance matched the maximum emission of the analyte from an average of two images taken when the pSiF reflectance maximum was at higher and lower

wavelengths showed the best ability to enhance the analyte without significant false positives being observed. The ability to be able to include multiple spectral features within one single filter that is tunable has also been demonstrated.

A larger wavelength shift of the rugate band than those reported in this paper is possible with a higher concentration of 2-propanol in the dosing chamber, but the rapid heating and cooling caused condensation to build up on the glass window under these conditions. An increased wavelength range could also be achieved by cooling the sample to lower temperatures during the thermal cycling, since this would allow greater capillary condensation of 2-propanol to occur. Modification of the initial fabrication parameters of the pSiF could lead to increases in the wavelength range accessible using this vapor condensation method. Thus, using a silicon substrate with higher resistivity can yield much larger spectral shifts in the rugate reflectance band, but it is far more challenging to create complex waveforms with sharp features ($\sim 10 \text{ nm fwhm}$) and with optical uniformity over a wide region in such material. Therefore, the current design with a 70 nm total tunable range and with *ca.* 30 nm controllable tunability represents a good first-generation demonstration of a tunable imaging filter based on reversible condensation of a volatile liquid into a nanoporous photonic crystal.

EXPERIMENTAL SECTION

Formation of Porous Silica Rugate Filters. Porous silicon rugate filter samples of 3.2 cm diameter were fabricated on single-crystalline highly doped p-type silicon wafers (0.90–1.20 $\text{m}\Omega\text{ cm}$ resistivity, (100)-polished, B-doped, from Siltronix Corporation) by electrochemical etch in a solution of 49% aqueous hydrofluoric acid (VWR)/ethanol (Rossville Gold Shield Chemical Company) (3:1 v/v), using a composite current density–time waveform. (CAUTION: HF is highly toxic and contact with skin should be avoided.) The composite waveform was a sum of three sine waves of amplitudes 10.42, 3.33, and 2.92 mA cm^{-2} with periods of 4.600, 4.430, and 4.425 s, respectively, superimposed on an offset current of 83.33 mA cm^{-2} , with 240 repeats. The start of the waveform was phase shifted 45° to decrease surface reflectivity. This waveform was empirically designed such that the reflectivity spectrum that resulted after oxidation of the porous silicon would overlap with the two main red bands of the sensitized europium photoluminescence spectrum. The waveform was generated using Igor Pro 6 software (Wavemetrics), and a Kepco power supply (ATE 25-2DM, 0–25 V, 0–2 A) under computer control (LabVIEW, National Instruments) was used to apply the composite waveform during the electrochemical etch. The resulting porous silicon was then partially oxidized at $600 \text{ }^\circ\text{C}$ for 55 min to increase stability.²⁷

Synthesis of Imaging Target $[\text{Ru}(\text{DMB})_3](\text{PF}_6)_2$. The ruthenium(II) complex of dimethylsulfoxide, $[\text{Ru}(\text{DMSO})_4]\text{Cl}_2$, was prepared as described by Evans *et al.*³³ The yellow flaky product was reacted with 3.2 equivalents of 4,4'-dimethyl-2,2'-bipyridine (DMB) in 95% ethanol and refluxed under nitrogen for 24 h. The solution was then reduced in volume, and a solution of 0.2 M NH_4PF_6 was added slowly with stirring to the boiling solution. The solution was then cooled to room temperature, and the resulting precipitate was filtered and rinsed with diethyl ether to yield a

red powder. A portion of the red powder was placed on a glass fiber filter for the imaging experiments.

Synthesis of Imaging Targets $[\text{Eu}(\text{dpa})_3]^{3-}$ and $\text{Eu}(\text{NO}_3)_3$. A solution of europium(III) tris-dipicolinate, $[\text{Eu}(\text{dpa})_3]^{3-}$, was prepared as described by Fernandes *et al.*³⁴ and was used without isolation. Briefly, europium(III) nitrate was refluxed in water with three equivalents of 2,6-pyridinedicarboxylic acid (dipicolinic acid, or dpaH₂) for 24 h. Both chemicals were used as received from Sigma Aldrich. The final solution was then added dropwise to a glass fiber filter and dried in a vacuum oven. This resulted in the $[\text{Eu}(\text{dpa})_3]^{3-}$ being both adsorbed within the filter and present as a white salt on the filter surface. A control sample was made using only $\text{Eu}(\text{NO}_3)_3$ deposited from an aqueous solution onto a glass fiber filter in a similar fashion. These samples were then used as targets in the imaging experiments.

Formation of Thermally Tunable Optical Filter and the Imaging System. The pSiF was placed into an airtight dosing chamber such that it was affixed to a stainless steel plate in contact with a Peltier cooler. The temperature was controlled using an FTC100 controller with a thermocouple and a FTX700 amplifier (Ferrotec Corporation). The backside of the Peltier device was contacted to a copper heat sink. A second thermocouple was attached to the frontside of the pSiF to monitor its temperature. The front window of the dosing chamber consisted of a piece of low-reflectance glass (Edmund Optics). Once assembled, the chamber was flushed with 2-propanol vapor (95 parts per thousand) until the reflectance peak reached a steady value, at which point the chamber was sealed. The Peltier temperature was programmed to cycle between 28 and $110 \text{ }^\circ\text{C}$, resulting in a $\sim 70 \text{ nm}$ shift of the porous silica rugate reflectance spectrum. Initial characterization of the optical behavior of the device used an Ocean Optics USB4000 spectrophotometer with reflectance probe. For imaging, a beam splitter was placed between the front of the pSiF cell and a Chameleon CMLN-13S2M monochrome

camera (Point Gray) equipped with a 50 mm double Gauss lens (Edmund Optics) (Figure 1). The surface where the dye targets were placed was orthogonal to the axis defined by the filter and camera. Two visible achromatic lenses ($f = 50.0$ mm, Thor Laboratories) were placed between the camera lens and the beamsplitter and the scene and the beamsplitter to focus the image onto a small (*ca.* 12.5 mm diameter) region of the pSiF.

Imaging and Data Processing. The imaging was conducted in the dark, with the only illumination being a long-wave ultraviolet lamp. The glass elements in the optical path, together with the pSiF and camera response, prevented this excitation light from appearing in the images. Camera images were acquired every 500 ms by means of a computer-controlled program (LabVIEW, National Instruments), while the temperature was cycled with a period of 135 s. A single “dark image” was acquired by imaging the scene without any UV illumination. Each monochrome image (stored as a 1280×960 , JPEG, 8-bit 3 channel image) was imported into MATLAB (The MathWorks, Inc.), and a single channel (all three channels contain the same information) was selected, cropped to 421×439 pixels, and subjected to a 3×3 spatial average. This reduced image size represents a target area of *ca.* 1.5×1.5 cm. Principal component analysis of the images corresponding to a single heat/cool cycle was performed using the MATLAB toolboxes PLS_Toolbox and MIA_Toolbox, both from Eigenvector Research, Inc., with no preprocessing apart from the 3×3 spatial average. To obtain the images in Figure 4, a dark image was then subtracted from images taken during thermal cycling to correct for stray illumination. All the images in the paper have each had global contrast adjustments.

The background correction results presented in this paper are based on three images taken at selected points during the thermal cycle that coincide with (1) the main pSiF reflectance band blue-shifted from coincidence with the main emission band of the $[\text{Eu}(\text{dpa})_3]^{3-}$ ($\text{Image}_{T_{\text{high}}}$); (2) the main pSiF reflectance band matching the wavelength of the $[\text{Eu}(\text{dpa})_3]^{3-}$ emission band ($\text{Image}_{T_{\text{match}}}$); and (3) the main pSiF reflectance band red-shifted from coincidence with the $[\text{Eu}(\text{dpa})_3]^{3-}$ emission band ($\text{Image}_{T_{\text{low}}}$) (Figure 4d). A background-corrected image that is selective for $[\text{Eu}(\text{dpa})_3]^{3-}$ can then be constructed by calculating a difference image using eq 1.³⁰

$$\text{Image}_{3\lambda} = \text{Image}_{T_{\text{match}}} - 0.5 \times (\text{Image}_{T_{\text{high}}} + \text{Image}_{T_{\text{low}}}) \quad (1)$$

where “ $\text{Image}_{3\lambda}$ ” is the resultant $[\text{Eu}(\text{dpa})_3]^{3-}$ -selective image. Images resulting from a subtraction of each of the single images $\text{Image}_{T_{\text{high}}}$ and $\text{Image}_{T_{\text{low}}}$ from the image corresponding to the maximum emission of $[\text{Eu}(\text{dpa})_3]^{3-}$ were also calculated (eqs 2 and 3) for comparison with the difference image calculated using eq 1.

$$\text{Image}_{2\lambda_{\text{high}}} = \text{Image}_{T_{\text{match}}} - \text{Image}_{T_{\text{high}}} \quad (2)$$

$$\text{Image}_{2\lambda_{\text{low}}} = \text{Image}_{T_{\text{match}}} - \text{Image}_{T_{\text{low}}} \quad (3)$$

The ROC curves were generated in MATLAB by defining a mask based on either the area of the glass fiber paper coated in $[\text{Eu}(\text{dpa})_3]^{3-}$ or the upper left region of interest in Figure 4b. Each image used for the ROC calculation was then thresholded using 100 threshold values between the image minimum and maximum pixel values. Comparison of these thresholded images with one of the two masks defined above allowed calculation of $p(\text{true positive})$ and $p(\text{false positive})$.

Conflict of Interest: The authors declare no competing financial interest.

Acknowledgment. This material is based upon work supported by the National Science Foundation under Grant No. DMR-1210417.

Supporting Information Available: SEM images showing the morphology of the porous silicon samples. This material is available free of charge via the Internet at <http://pubs.acs.org>.

REFERENCES AND NOTES

- Hiraoka, Y.; Shimi, T.; Haraguchi, T. Multispectral Imaging Fluorescence Microscopy for Living Cells. *Cell Struct. Funct.* **2002**, *27*, 367–374.
- Levenson, R. M.; Mansfield, J. R. Multispectral Imaging in Biology and Medicine: Slices of Life. *Cytometry, Part A* **2006**, *69A*, 748–758.
- Chamberland, M.; Belzile, C.; Farley, V.; Legault, J.-F.; Schwantes, K. R. In *Advancements in Field-Portable Imaging Radiometric Spectrometer Technology for Chemical Detection*; Gardner, P. J., Ed.; SPIE: Orlando, FL, USA, 2004; pp 63–72.
- Lagueux, P.; Vallieres, A.; Villemaire, A.; Chamberland, M.; Farley, V.; Giroux, J. In *Chemical Agent Standoff Detection and Identification with a Hyperspectral Imaging Infrared Sensor*; Berlin, Germany; Lewis, C., Ed.; SPIE: Berlin, Germany, 2009; pp 74860C–12.
- Goetz, A. F. H.; Curtiss, B. Hyperspectral Imaging of the Earth: Remote Analytical Chemistry in an Uncontrolled Environment. *Field Anal. Chem. Technol.* **1996**, *1*, 67–76.
- Gupta, N.; Ashe, P. R.; Tan, S. Miniature Snapshot Multispectral Imager. *Opt. Eng.* **2011**, *50*, 033203–9.
- Staromlynska, J.; Rees, S. M.; Gillyon, M. P. High-Performance Tunable Filter. *Appl. Opt.* **1998**, *37*, 1081–1088.
- Morris, H. R.; Hoyt, C. C.; Treado, P. J. Imaging Spectrometers for Fluorescence and Raman Microscopy: Acousto-Optic and Liquid Crystal Tunable Filters. *Appl. Spectrosc.* **1994**, *48*, 857–866.
- Sutherland, R. L.; Mathger, L. M.; Hanlon, R. T.; Urbas, A. M.; Stone, M. O. Cephalopod Coloration Model. I Squid Chromatophores and Iridophores. *J. Opt. Soc. Am. A* **2008**, *25*, 588–599.
- Biro, L. P.; Vigneron, J.-P. Photonic Nanoarchitectures in Butterflies and Beetles: Valuable Sources for Bioinspiration. *Laser Photonics Rev.* **2011**, *5*, 27–51.
- Potyrailo, R. A.; Ghiradella, H.; Vertiatchikh, A.; Dovidenko, K.; Cournover, J. R.; Olsen, E. Morpho Butterfly Wings Demonstrate Highly Selective Vapour Response. *Nat. Photonics* **2007**, *1*, 123–128.
- Sailor, M. J.; Link, J. R. Smart Dust: Nanostructured Devices in a Grain of Sand. *Chem. Commun.* **2005**, 1375–1383.
- Li, Y. Y.; Cunin, F.; Link, J. R.; Gao, T.; Betts, R. E.; Reiver, S. H.; Chin, V.; Bhatia, S. N.; Sailor, M. J. Polymer Replicas of Photonic Porous Silicon for Sensing and Drug Delivery Applications. *Science* **2003**, *299*, 2045–2047.
- Tkachenko, G. V.; Tkachenko, V.; De Stefano, L.; Sukhoivanov, I. A. Tunable NIR Filter Based on a Free-Standing Porous Silicon Film Containing Nematic Liquid Crystal. *J. Opt. A-Pure Appl. Opt.* **2009**, *11*, 105106.
- Weiss, S. M.; Fauchet, P. M. Thermal Tuning of Silicon-Based One-Dimensional Photonic Bandgap Structures. *Phys. Status Solidi C* **2005**, *2*, 3278–3282.
- Poborchii, V. V.; Tada, T.; Kanayama, T. A Visible-Near Infrared Range Photonic Crystal Made Up of Si Nanopillars. *Appl. Phys. Lett.* **1999**, *75*, 3276–3278.
- Tetreault, N.; Miguez, H.; Ozin, G. A. Silicon Inverse Opal - a Platform for Photonic Bandgap Research. *Adv. Mater.* **2004**, *16*, 1471–1476.
- Ilyas, S.; Böcking, T.; Kilian, K.; Reece, P. J.; Gooding, J.; Gaus, K.; Gal, M. Porous Silicon Based Narrow Line-Width Rugate Filters. *Opt. Mater.* **2007**, *29*, 619–622.
- Berger, M. G.; Dieker, C.; Thonissen, M.; Vescan, L.; Luth, H.; Munder, H.; Theiss, W.; Wernke, M.; Grosse, P. Porosity Superlattices - a New Class of Si Heterostructures. *J. Phys. D: Appl. Phys.* **1994**, *27*, 1333–1336.
- Meade, S. O.; Yoon, M. S.; Ahn, K. H.; Sailor, M. J. Porous Silicon Photonic Crystals as Encoded Microcarriers. *Adv. Mater.* **2004**, *16*, 1811–1814.
- Sailor, M. J. *Porous Silicon in Practice: Preparation, Characterization and Applications*; Wiley-VCH: Weinheim, Germany, 2011; p 94.
- Weiss, S. M.; Ouyang, H.; Zhang, J.; Fauchet, P. M. Electrical and Thermal Modulation of Silicon Photonic Bandgap Microcavities Containing Liquid Crystals. *Opt. Express* **2005**, *13*, 1090–1097.
- Snow, P. A.; Squire, E. K.; Russell, P. S. J.; Canham, L. T. Vapor Sensing Using the Optical Properties of Porous Silicon Bragg Mirrors. *J. Appl. Phys.* **1999**, *86*, 1781–1784.

24. Pellegrino, P. M.; Fell, N. F.; Rosen, D. L.; Gillespie, J. B. Bacterial Endospore Detection using Terbium Dipicolinate Photoluminescence in the Presence of Chemical and Biological Materials. *Anal. Chem.* **1998**, *70*, 1755–1760.
25. Jenkins, A. L.; Murray, G. M. Ultratrace Determination of Selected Lanthanides by Luminescence Enhancement. *Anal. Chem.* **1996**, *68*, 2974–2980.
26. Ref 21, p 89.
27. Ruminski, A. M.; King, B. H.; Salonen, J.; Snyder, J. L.; Sailor, M. J. Porous Silicon-Based Optical Microsensors for Volatile Organic Analytes: Effect of Surface Chemistry on Stability and Specificity. *Adv. Funct. Mater.* **2010**, *20*, 2874–2883.
28. Koshida, N.; Nakajima, T.; Yoshiyama, M.; Ueno, K.; Nakagawa, T.; Shinoda, H. Ultrasound Emission from Porous Silicon: Efficient Thermoacoustic Function as a Depleted Nanocrystalline System. *Proc. Mater. Res. Soc.* **1999**, *105*–110.
29. Lee, J.-H.; Galli, G. A.; Grossman, J. C. Nanoporous Si as an Efficient Thermoelectric Material. *Nano Lett.* **2008**, *8*, 3750–3754.
30. Miskelly, G. M.; Wagner, J. H. Using Spectral Information in Forensic Imaging. *Forensic Sci. Int.* **2005**, *155*, 112–118.
31. Hsiao, C. N.; Chen, H. P.; Chiu, P. K.; Cho, W. H.; Lin, Y. W.; Chen, F. Z.; Tsai, D. P. Design and Fabrication of Optical Thin Films for Remote Sensing Instruments. *J. Vacuum Sci. Technol. A* **2010**, *28*, 867–872.
32. Gittins, C. M.; Marinelli, W. J. In *AIRIS Multispectral Imaging Chemical Sensor*, Orlando, FL, USA; Fallahi, M.; Howden, E. A., Eds.; SPIE: Orlando, FL, USA, 1998; pp 65–74.
33. Evans, I. P.; Spencer, A.; Wilkinson, G. Dichlorotetrakis-(dimethyl sulphoxide)ruthenium(II) and its Use as a Source Material for Some New Ruthenium(II) Complexes. *J. Chem. Soc., Dalton Trans.* **1973**, 204–209.
34. Fernandes, A.; Jaud, J.; Dexpert-Ghys, J.; Brouca-Cabarrecq, C. Study of New Lanthanide Complexes of 2,6-Pyridinedicarboxylate: Synthesis, Crystal Structure of Ln(Hdipic)(dipic) with Ln = Eu, Gd, Tb, Dy, Ho, Er, Yb, Luminescence Properties of Eu(Hdipic)(dipic). *Polyhedron* **2001**, *20*, 2385–2391.